

SUMER OBSERVATIONS OF THE QUIET-SUN TRANSITION REGION

N. W. GRIFFITHS,¹ G. H. FISHER, D. T. WOODS,² AND O. H. W. SIEGMUND¹

Space Sciences Laboratory, University of California, Berkeley, Berkeley, CA 94720-7450;
neilg@ssl.berkeley.edu, fisher@ssl.berkeley.edu, tod@eaglevail.llnl.gov, ossy@ssl.berkeley.edu

Received 1998 April 23; accepted 1998 September 28

ABSTRACT

We present new results from observations of the quiet Sun taken with the SUMER spectrograph on the *SOHO* spacecraft. This study includes line and continuum emission covering a wide range of temperatures, and the data have been used to create a number of intensity maps with a field of view of $\sim 60'' \times 300''$ and a spatial resolution of $\sim 1''$. These maps reveal bright features that extend from ~ 6000 K to ~ 2 MK, indicating that much of the observed transition region emission arises in an atmospheric interface between the chromosphere and corona. The emission-line intensities over our field of view vary by up to 2 orders of magnitude and have lognormal distributions suggestive of small-scale magnetic fragmentation. We find empirical evidence for a power-law relationship between line emission and electron density, with an exponent in the range ~ 0.3 – 1.0 . Possible temperature dependence of the exponent is reflected in the slope of the emission measure curve, which appears to change slightly with varying electron density. However, there is no major variation in the shape of the lower transition region emission measure distribution with either the intensity or the size of the area studied. This indicates that ensembles of “cool loops” (loops physically distinct from those structures which reach coronal temperatures) are unlikely to be the source of this emission unless the size of the structures is considerably less than $1''$. We also find that the Li-sequence N v $\lambda 1240$ emission is higher than expected, in agreement with several previous studies. It seems that this effect diminishes with intensity, suggesting that it is unlikely to be due to the omission of density dependence in dielectronic recombination calculations.

Subject headings: Sun: transition region — Sun: UV radiation

1. INTRODUCTION

The physics of the solar chromosphere-corona transition region has been widely investigated and has relied upon observations in the EUV and UV wavelength bands. Prior to the launch of the *Solar and Heliospheric Observatory (SOHO)*, some of the best transition region spectra were obtained by the Naval Research Laboratory (NRL) S082-B EUV spectrograph (Bartoe et al. 1977), which was flown on the *Skylab* space station. The S082-B instrument covered the wavelength range 970–3940 Å. It had a spectral resolution of about 0.05 Å at 1500 Å but a rather modest spatial resolution of $2'' \times 60''$. These *Skylab* spectra proved most useful for plasma diagnostics of spatially averaged solar regions. Several of these observations are discussed by Doschek (1997) and references therein. High spectral resolution observations of the solar transition region were also obtained using the NRL High-Resolution Telescope Spectrograph (HRTS) (Brueckner, Bartoe, & VanHoosier 1977; Brueckner & Bartoe 1983). The HRTS featured much better spatial resolution ($\sim 1''$) than the *Skylab* observations. It has been used in a series of rocket experiments and was also flown on *Spacelab 2* (Brueckner et al. 1986).

The data obtained from the *Skylab* and HRTS experiments have been used to investigate many different characteristics of the solar transition region, and a thorough review of current knowledge is given by Mariska (1992). In the following paragraphs we briefly discuss some features of the transition region relevant to our SUMER observations.

One of the fundamental descriptions of the transition region comes from the distribution of emission measure with temperature (see § 6 for details). There has been con-

siderable consistency in the emission measure distributions derived for the quiet Sun (e.g., Raymond & Doyle 1981; Dere & Mason 1993; Doschek 1997). Typically, the emission measure decreases steadily from chromospheric temperatures to a minimum at $\log T_e \simeq 5.0$ – 5.2 . The emission measure then increases up to a peak in the corona at $\log T_e \simeq 6.2$ and falls off again at higher temperatures. The smooth variation of the emission measure as a function of temperature suggests there is some continuity in the outer solar atmosphere. Transition region models based on this interpretation have been discussed by Athay (1976) and Gabriel (1976). However, the change in gradient of empirical emission measure distributions may indicate some important differences in the energy transport processes above and below $\log T_e \simeq 5.0$ (Athay 1982). Feldman (1983) used this and other characteristics of the transition region to argue that the majority of the emission in the range $4.5 \lesssim \log T_e \lesssim 5.3$ did not arise from an intermediate layer in a stratified atmosphere but was instead emitted by what were termed “unresolved fine structures” (UFS). The UFS model was extended to higher temperatures by Feldman (1987) and Feldman & Laming (1994). Spadaro, Lanza, & Antiochos (1996) have proposed models for UFS, but these failed to reproduce some of the observational characteristics. Recently, the UFS model has been discussed by Wikstøl, Judge, & Hansteen (1998). They investigate the problems involved with unresolved dynamics in the solar atmosphere and conclude that the UFS model is unlikely to be the correct interpretation for the majority of the transition region emission.

Any detailed study of the transition region structure requires a knowledge of the plasma pressure, which is usually determined from density-sensitive line ratios. Some of the most useful diagnostics are the O IV $\lambda 1400$ multiplet (Cook et al. 1995; Brage, Judge, & Brekke 1996), lines of

¹ Experimental Astrophysics Group.

² Also Lawrence Livermore National Laboratory, L-15, P.O. Box 808, Livermore, CA 94550.

Si III (Dufton & Kingston 1994), and lines of C III (Berrington 1984). Using these lines, the electron pressure in the quiet Sun is typically found to be about 0.08–0.14 dynes cm^{-2} (Jordan 1996). However, an important conclusion from previous density-diagnostic work involves the level of uncertainty that can occur in line ratios. Jordan (1996) therefore stresses that ideally lines from the same element, at the same stage of ionization, and with similar wavelengths should be used. Doschek (1997) suggests that errors of the order of a factor of 2 can be introduced in line ratios through the many theoretical and observational parameters involved in the calculations. Furthermore, there are difficulties when inferring a single density from observations of a plasma with inhomogeneous density. This problem has been discussed for an isothermal plasma by Almléay, Brown, & Sweet (1989). They conclude that the spectroscopic mean density determined from a single line ratio will be *higher* than the true volumetric mean density. In other words, the inferred volume of the emitting plasma is always *less* than the true volume. This has important consequences for the apparent filling factor of the transition region, which is discussed below.

Several studies have combined limb observations, disk observations, and measured plasma pressures to indicate that transition region emission arises from a restricted portion of the solar surface. (As emphasized by Jordan 1996, the derived filling factors are often model dependent.) Dere, Bartoe, & Brueckner (1984) discuss HRTS data and find that the network at 10^5 K covers about 16% of the solar surface. However, Feldman, Doschek, & Mariska (1979) suggest that only about 1% of the solar surface is covered by spicular-type transition region emission over the chromospheric network. Dere et al. (1984) interpret this smaller filling factor as evidence for subresolution structures in the transition region and place an upper limit on the volume of such objects of 7×10^{21} cm^3 . Further evidence for subresolution filamentation is given by Dere (1982), and spicular structure filling factors of 10^{-5} to 10^{-2} have been suggested by Dere et al. (1987). This topic has also been discussed by Jordan (1996).

One of the most intriguing features of the solar transition region is that emission lines often exhibit significant redshifts, with velocities of up to 20 km s^{-1} in active regions. The variation of redshift with temperature has been investigated by a number of authors (e.g., Doschek, Feldman, & Bohlin 1976; Achour et al. 1995; Chae, Yun, & Poland 1998) and appears to reach a maximum at $\log T_e \simeq 5.1$ – 5.3 . A number of models have been suggested to explain this phenomenon, such as flows and episodic heating (see Achour et al. 1995 and references therein) or acoustic waves (Hansteen 1993), but at present the precise origin of the observed redshifts remains uncertain.

It is clear that our understanding of the solar transition region will be enhanced by new observations with high spectral and spatial resolution. The Solar Ultraviolet Measurements of Emitted Radiation (SUMER) instrument (Wilhelm et al. 1995) on *SOHO* therefore provides an excellent opportunity to study many of the transition region characteristics discussed above. SUMER features a spectral resolution of ~ 43 $\text{m}\text{\AA}$ in first order, ~ 22 $\text{m}\text{\AA}$ in second order, and a spatial resolution of $\sim 1''$. It can cover wavelengths from 330 to 1610 \AA , depending on the spectral order and the choice of detector. The first results from SUMER are summarized by Wilhelm et al. (1997) and Lemaire et al.

(1997), and with relatively few exceptions the instrument is performing up to its prelaunch specifications. We have prepared and run a SUMER observing sequence that includes a range of transition region emission lines in the temperature range $4.7 \lesssim \log T_e \lesssim 5.4$ plus a coronal line of Fe XII. The observations also include continuum emission from the chromosphere. This data set is ideal for investigating much of the solar transition region, and in this paper we discuss a number of results based on our observations.

2. SUMER OBSERVATIONS AND DATA REDUCTION

We obtained extended SUMER observations of the quiet Sun on 1997 March 18. The study used the $1'' \times 300''$ slit and lasted from UT 00:31 to UT 07:20. The default detector at the time of the observations was detector B (see Wilhelm et al. 1995). Our SUMER observations include lines from N II, N III, N IV, and N V, formed over the temperature range $4.7 \lesssim \log T_e \lesssim 5.3$, and lines from O II, O III, O IV, and O V, which are formed in a similar temperature range. By confining our attention to lines from only two elements, the effects of elemental abundance variations in the transition region are minimized. We also observed the O IV] $\lambda 1400$ density-sensitive multiplet to obtain an independent measure of the transition region pressure (the formation temperature for O IV of $\log T_e = 5.25$, plus the derived density, allows us to infer the pressure). However, SUMER operating restrictions prevented us from including the O VI lines at 1031.9 and 1037.6 \AA .

At the time of our observations, the SUMER slit-scanning (raster) mechanism had been disabled. The observations were therefore taken with the slit fixed at disk center and the Sun rotating through our field of view. The lines were split into four wavelength bands, and each band was subject to repeated 60 s exposures. A list of the observed emission lines in each band is given in Table 1. (A coronal line of Fe XII is also included.) As time evolves, an image of the Sun is built up as it rotates through our slit position. The time between subsequent exposures in each emission line is about 6.7 minutes. In this time the Sun will have rotated by about 800 km at the equator, corresponding to an angle subtended at *SOHO* of about $1''.1$. Therefore, the intensity maps we build up have almost the same aspect ratio as a true image. Our observation lasted a total of ~ 7 hr, corresponding to 60 exposures in each line. For each spectral line observed, therefore, we can create a spatial image with a field of view $\simeq 60'' \times 300''$. These images are discussed further in § 3.

The nature of our observations deserves a brief discussion. Since the data were taken with the Sun rotating under the slit, each band of emission lines corresponds to slightly different regions of the solar surface. In particular, the fields of view corresponding to the first and fourth bands in the same pixel only overlap by about 40%. There is consequently some variation in the absolute longitudinal position of intensity maps made in emission lines from different bands. However, we suggest that this will not have a significant effect on our conclusions. The differences in position are $\lesssim 0''.6$, and we shall see in § 3 that the autocorrelation functions for our images only decrease modestly over $1''$. In § 5 we investigate line fluxes from pixels binned by both intensity and spatial position. The intensity bins contain 1800 pixels, and many of the pixels in each bin will be clustered together in subregions. The effects of our positional variations are therefore unimportant.

TABLE 1
SUMER OBSERVATIONS: STUDY BANDS AND EMISSION LINES

BAND 1		BAND 2		BAND 3		BAND 4	
Ion	λ (Å)	Ion	λ (Å)	Ion	λ (Å)	Ion	λ (Å)
O v	760.228	O II	833.332	N v	1238.821	O IV]	1399.774
O v	760.445	O II	834.462	N v	1242.804	O IV]	1401.156
N III	764.357	O III	833.742	Fe XII	1242.010	O IV] ^a	1404.812
N IV	765.143	O IV] ^b	1407.386
N II	775.965
O IV	787.711

^a Blended with S IV λ 1404.770.

^b Blended with O III λ 703.850 in second order.

The flat-field correction was performed during the data reduction process, using a flat-field image created at the same time as our observations. (Automatic in-flight flat-fielding was also available). No data compression was used in the telemetry to minimize losses. Since the SUMER optics lead to wavelength-dependent variations in the size of the slit on the detector, all our data sets were normalized to a length of 300 pixels (i.e., 300") in the spatial direction. Each line profile was studied as a function of time, so that the position of the line on the detector and the level of the background could be accurately determined. Line intensities were found by summing the counts in a given emission feature, subtracting the local background, and applying the laboratory calibration of detector B corrected for the in-flight decrease in sensitivity due to operations at low gain. Integrating the intensities over 2π sr gives surface fluxes ($\text{ergs cm}^{-2} \text{s}^{-1}$). Total emission-line powers were determined by integrating surface fluxes over the observed area and then multiplying by 2 (half the emission is radiated downward).

3. SUMER INTENSITY MAPS

As described in § 2, we can construct spatial images for each emission line in our study. The images for our observed emission lines are shown in Figure 1. We also show images made in the C I continuum (taken next to the N v λ 1238.8 line) and in the Lyman continuum (taken next to the O IV λ 787.7 line). The C I and Lyman continua are formed at about 6000 and 8000 K, respectively (~ 1000 and ~ 2000 km above $\tau_{5000} = 1$), in the solar atmosphere (Vernazza, Avrett, & Loeser 1973). It is important to note that the generally brighter images in the weak N II and Fe XII lines are indicative of the limited dynamic range, due to a low signal-to-noise ratio, rather than a higher level of "diffuse" emission.

The most striking aspect of these images is that many of the brightest features appear in images of the chromosphere (e.g., C I continuum, $\log T_e = 3.8$), the lower transition region (e.g., N II, $\log T_e = 4.7$), the upper transition region (e.g., O v, $\log T_e = 5.4$), and the corona (Fe XII, $\log T_e = 6.2$). This indicates that emission over a wide range of temperatures is arising from the same set of structures. There is clear continuity in these structures throughout the outer solar atmosphere, and a gravitationally stratified model is probably most appropriate. This is in obvious conflict with the suggestion of Feldman (1983, 1987) and Feldman & Laming (1994) that the majority of the transition region emission comes from "unresolved fine structures" distinct

and separate from the physical interface between the chromosphere and corona. As discussed in § 4, a large fraction of the total emission in our images comes from the brightest pixels. It is precisely these features that show a clear continuity throughout the atmosphere. However, there are also some features that appear much more prominently in the upper transition region images (e.g., the small, bright point toward the upper left-hand corner of the N v, O IV, and O v images). It is likely that a number of different processes and structures will contribute to the transition region emission. The nonuniqueness of models inferred from observations is discussed by Wikstøl et al. (1998), and we accept this as a caveat to our general conclusion.

It is interesting to compare the C I and Lyman continuum maps. The C I image shows many small, discrete bright features that are not seen in the Lyman continuum map or the transition region images. Although the two chromospheric images are formed at similar temperatures, the C I continuum originates about 1000 km below the Lyman continuum in the solar atmosphere (Vernazza et al. 1973). A possible explanation is that there is a significant expansion of the magnetic structures between the formation levels of the C I and Lyman continua.

We can investigate the scale of the visible features through the autocorrelation of the intensity maps. It is preferable to do this using data from the oxygen lines, since these generally have higher count rates than the nitrogen lines. We compute the autocorrelations of the two-dimensional intensity maps. The spatial size in Figure 2 is quoted in pixels, but we note that there is a slight difference ($\sim 10\%$) in the pixel "size" in each dimension (see § 2). In Figure 2a we show the autocorrelations of intensity maps in O II, O III, O IV, O v, and Fe XII. The visual similarity of the transition region maps in Figure 1 is reinforced by the close agreement of the autocorrelation coefficients for the strong O II, O III, O IV, and O v λ 760.4 lines. It is clear that the structures responsible for transition region emission do not vary significantly from $\log T_e = 4.7$ to $\log T_e = 5.4$. The coefficient of the coronal Fe XII line drops off much more rapidly than the coefficients of the strong transition region lines. However, there is also a clear difference in the autocorrelation of the strong O v λ 760.4 line and the weak O v λ 760.2 line. This suggests that the Fe XII coefficient is affected by the large pixel-to-pixel variations arising from the low signal-to-noise ratio in this line. Therefore, the Fe XII coefficient cannot be used to infer differences between the coronal and transition region structures. In Figure 2b we compare the autocorrelation coefficient of the O IV tran-

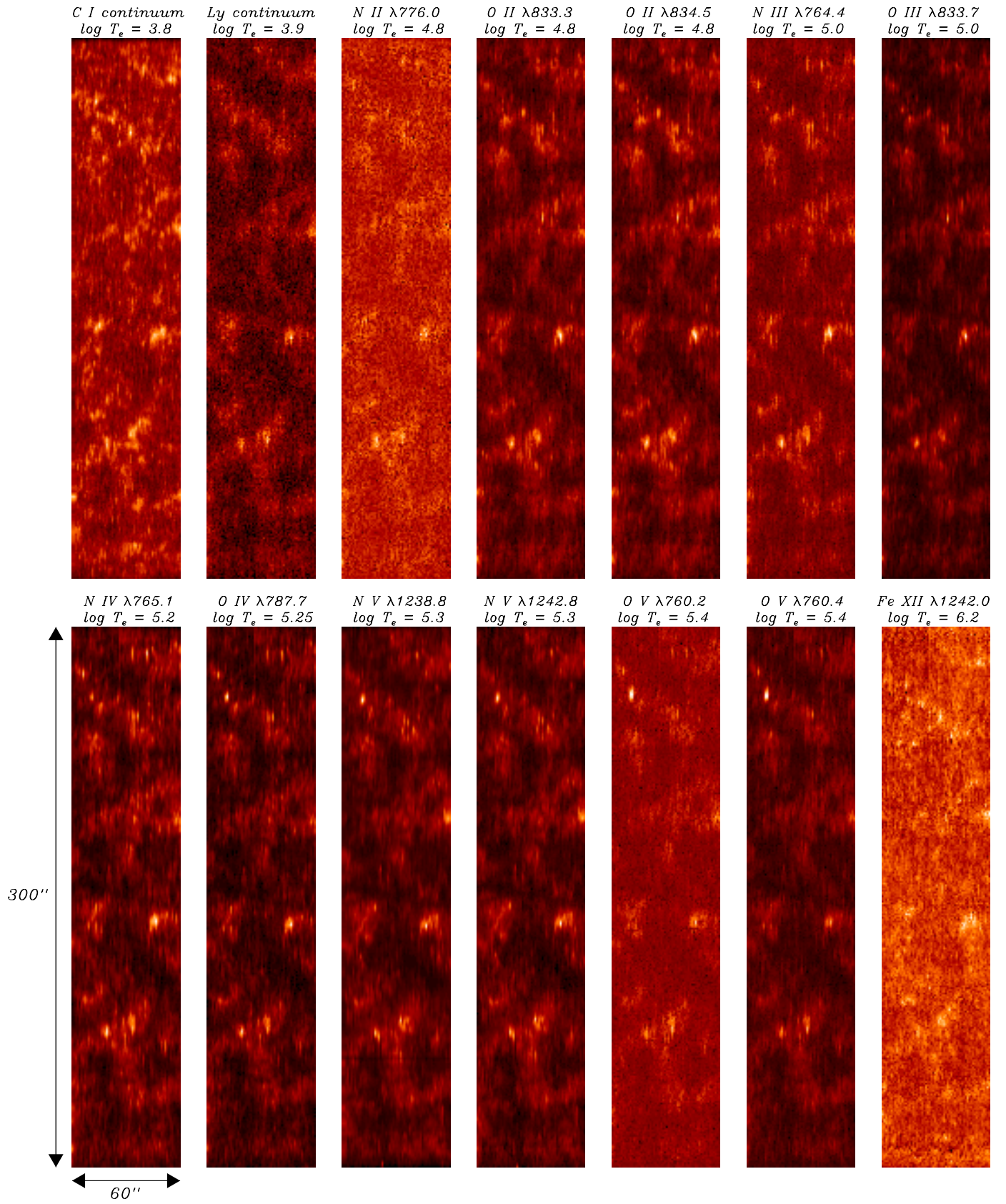


FIG. 1.—SUMER intensity maps

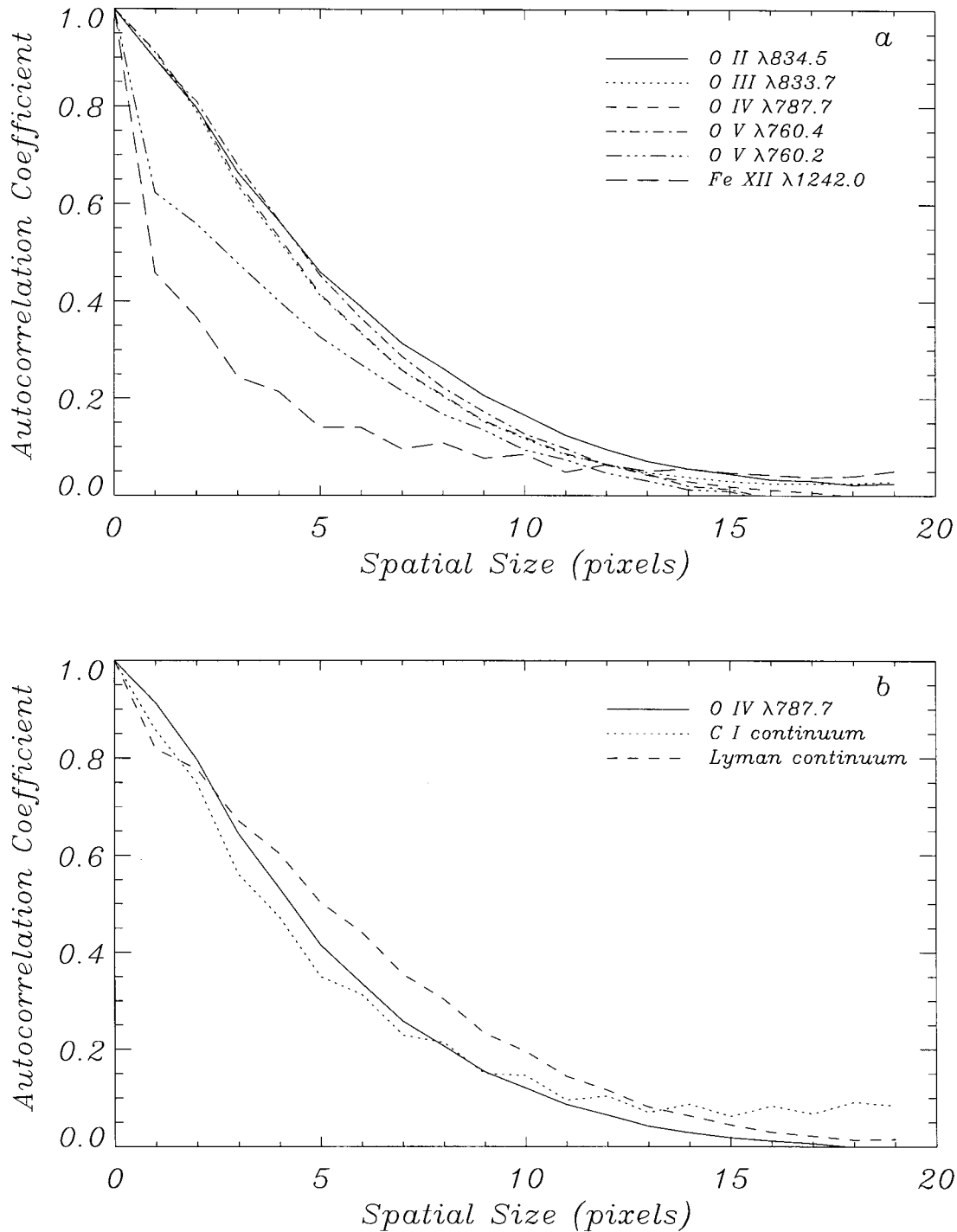


FIG. 2.—(a) Autocorrelation coefficients for intensity maps in the transition region and corona. Note that 1 pixel $\approx 1''$ at L1. (b) A comparison of the autocorrelation coefficients for the $O\ IV\ \lambda 787.7$ transition region intensity map and the chromospheric $C\ I$ continuum and Lyman continuum intensity maps.

sition region map with the coefficients of the chromospheric maps made in the $C\ I$ continuum and the Lyman continuum. The general agreement between the transition region and the chromosphere is good, especially for the $C\ I$ continuum.

4. THE DISTRIBUTION OF INTENSITY

The intensity distribution functions for all the lines in our study are shown in Figure 3. We see that the emission-line intensities vary by about 2 orders of magnitude over our

field of view. Furthermore, it seems that a large fraction of the total emission comes from a relatively small number of pixels. For example, 50% of the total intensity in $N\ IV\ \lambda 765.1$ comes from about 7% of the area. Similar restricted patterns of emission were seen in the $C\ IV\ \lambda\lambda 1548, 1550$ transition region lines by Dere et al. (1984) and in observations of the chromospheric network by Reeves (1976).

Figure 3 indicates that the pixel brightness for all the lines in our study is lognormally distributed. Similar distributions have been recorded for a wide range of SUMER

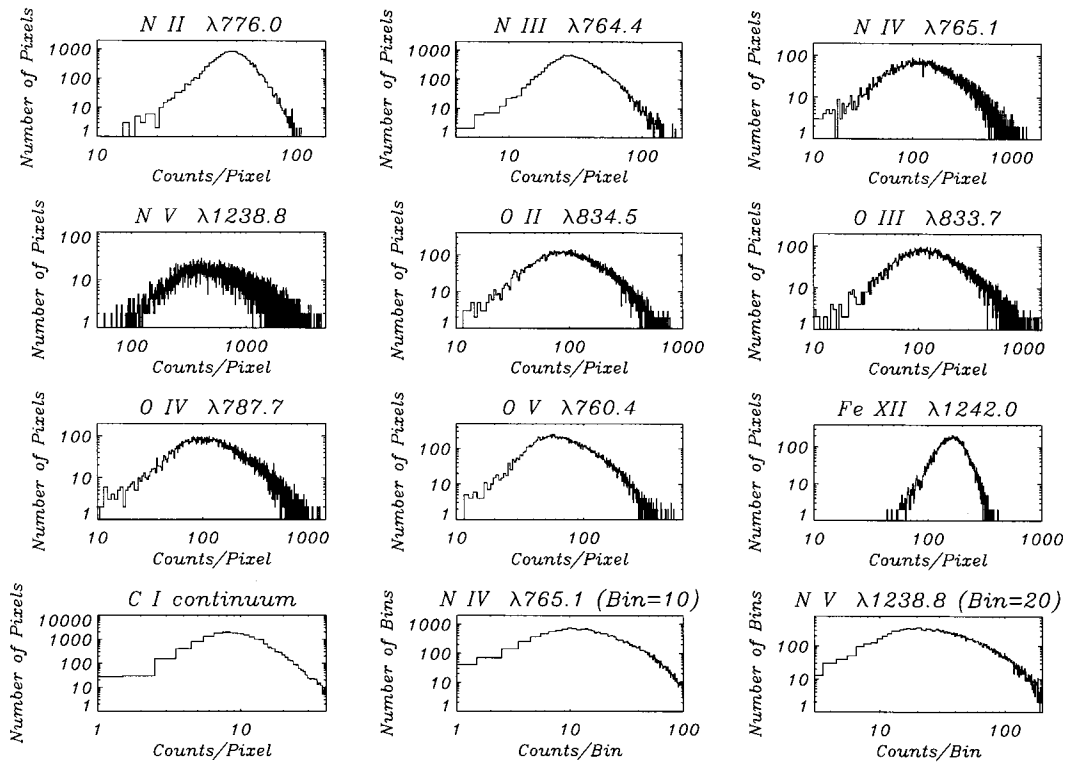


FIG. 3.—Intensity distribution functions for the observed emission lines and the C I continuum. We also show histograms for N IV and N V, where the number of counts per pixel has been binned. The factor by which the counts have been binned is indicated on each histogram.

observations (I. E. Dammasch 1997, private communication). This may suggest that the emission is associated with small, fragmenting magnetic elements: Bogdan et al. (1988) and Berger et al. (1995) discuss such processes with reference to sunspot areas and photospheric bright points, respectively. A discussion of how fragmentation mechanisms lead to lognormal distributions is given in Bogdan (1992). We note that the distributions for lines with the largest count rates appear “noisy” (e.g., N IV, N V, O III, and O IV). This effect can be reduced by binning the number of counts per pixel, and we include binned histograms for N IV and N V in Figure 3. However, this approach tends to flatten the distributions, and their true shape becomes less obvious.

We also show the intensity distribution function for the chromospheric C I continuum. (The Lyman continuum data have insufficient counts for a useful distribution function to be derived.) The C I continuum distribution appears to be lognormal, similar to the transition region emission lines. This could be further evidence of a physical connection between the structures responsible for the chromospheric and transition region emission.

5. TRANSITION REGION PRESSURES

Our observations included measurements of the O IV] $\lambda 1400$ multiplet. Ratios of lines in this multiplet can in principle yield values for the electron density (Cook et al. 1995; Brage et al. 1996). In practice, there are problems associated with two of these lines. The $\lambda 1404.8$ line is blended with S IV $\lambda 1404.8$, and in SUMER spectra the $\lambda 1407.4$ line is blended with the O III $\lambda 703.9$ line in second order. We therefore prefer using the $\lambda 1399.8/\lambda 1401.2$ ratio. Cook et al. (1995) calculated the theoretical value of this ratio as a function of electron density. Using a measured value of the line ratio

from some observed region, we can determine an average electron density for that region by interpolating on the theoretical curve (e.g., Fig. 1 of Cook et al. 1995). Averaged over the whole observation, the $\lambda 1399.8/\lambda 1401.2$ line ratio has a value of 0.183 ± 0.013 . This corresponds to an electron density of $\log N_e = 9.60^{+0.27}_{-0.56}$ and an electron pressure of $P_e = 0.09$ dynes cm^{-2} . The uncertainties are large, because in this regime N_e is a very rapidly changing function of the line ratio.

The O III $\lambda 703.9$ blend with O IV] $\lambda 1407.4$ can be estimated using the clean O III line at 833.7 Å. Using the CHIANTI database (Dere et al. 1997), the $\lambda 703.9/\lambda 833.7$ ratio was determined and found to be almost constant over the expected density range for the quiet Sun. The contribution in detector counts of the $\lambda 703.9$ line to the blended profile was then estimated, and a corrected O IV] flux was determined. The O IV] $\lambda 1407.4$ line is predicted to account for $\sim 14\%$ of the counts in the combined feature, and the $\lambda 1407.4/\lambda 1401.2$ line ratio suggests a density of $\log N_e = 9.64$ and a pressure of $P_e = 0.10$ dynes cm^{-2} . This agrees well with the $\lambda 1399.8/\lambda 1401.2$ estimate.

The electron pressures we derive are similar to previous measurements of the solar transition region (Jordan 1996). However, we do see evidence for density inhomogeneity in our data set. In Figure 4 we examine data from spatial subregions of our observations. The top panel shows the total power in the O V $\lambda 760.4$ line integrated over the $300''$ length of the slit and over groups of three exposures. The resulting plot shows the total O V $\lambda 760.4$ counts for 20 exposure bins. The middle panel shows the O IV] $\lambda 1399.8/\lambda 1401.2$ line ratio when both data sets have been binned in the same way as above. The bottom panel shows the electron density inferred from the binned line ratio array. Figure 4 suggests some spatial correlation between intensity

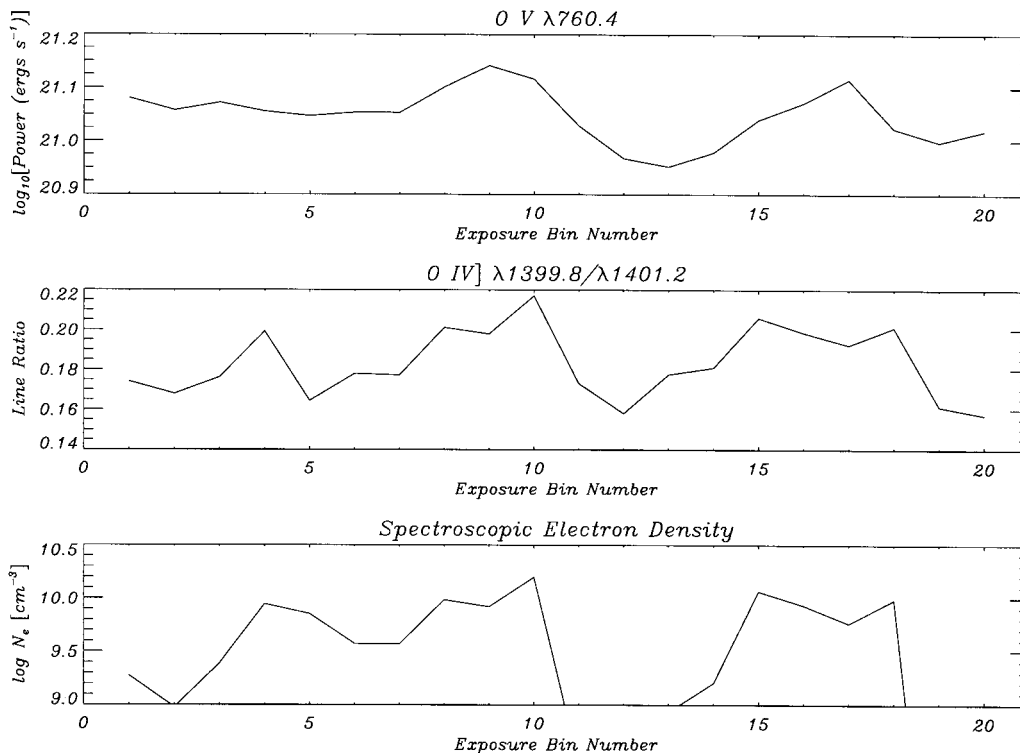


FIG. 4.—(a) Variation of the total power in the O v $\lambda 760.4$ line for binned exposures. (An “exposure bin” is a group of three consecutive exposures.) (b) Variation of O IV] $\lambda 1399.8/\lambda 1401.2$ line ratio for binned exposures. (c) Variation of $\log N_e$ for binned exposures.

and electron density, although the evidence is rather qualitative.

A clearer indication of a correlation is given in Figure 5. We compare the total power in the line with electron density for 10 different intensity bins in each emission line. The electron density is determined at the formation temperature of O IV ($\log T_e \sim 5.25$) from the O IV] $\lambda 1399.8/\lambda 1401.2$ line ratio. The dashed lines show the best linear fit to the points, based on minimizing the χ^2 error statistic. For some lines these fits rely on rejection of apparently spurious points, where the O IV] line ratio is at or below the low-density limit (corresponding to $\log N_e = 8.0$). In these cases we also make fits that use all the points, including those at the low-density limit. These fits are shown as dotted lines.

From Figure 5 it appears that the total power in each emission line can be expressed in the form

$$P = CN_e^\nu, \quad (1)$$

where C and ν are constant for a given line. In Table 2 we list the values of C and ν for each emission line, taken from the fits given in Figure 5. The values of C in Table 2 are determined over the area of one intensity bin, i.e., 1800 square pixels. Since the pressure in the transition region is approximately constant, the value of ν for transition region lines is largely independent of the temperature at which N_e is determined (although the value of C will change). However, it is not clear how the pressure varies between the formation temperatures of O IV and Fe XII. The physical significance of the value of ν derived for the Fe XII line is therefore uncertain.

We see that the exponent ν is typically between ~ 0.3 and ~ 1.0 . The variation of ν with temperature is shown in Figure 6. There is evidence for a peak in the value of ν at $\log T_e = 5.0$, but the uncertainties are significant. Jordan et

al. (1987) studied IUE data for five G–K dwarfs, and found empirical evidence for a value of $\nu = 0.9$ when comparing pressure and the combined intensity of Si IV ($\log T_e = 4.8$), C IV ($\log T_e = 5.0$), and N V ($\log T_e = 5.3$). The two lower temperature lines dominate the combined intensity, but the exponent is still a little higher than our solar values predict.

TABLE 2
FIT PARAMETERS FOR EMISSION-LINE POWER $P = CN_e^\nu$

Ion	$\log T_e^a$	λ	C^b	ν
N II	4.7	776.0	14.506 ± 5.832	0.594 ± 0.611
N III	5.0	764.4	9.237 ± 4.500	1.197 ± 0.472
N IV	5.2	765.1	14.439 ± 1.290	0.776 ± 0.137
N V	5.3	1238.8	17.175 ± 1.596^c	0.495 ± 0.165^e
			19.169 ± 0.462^d	0.291 ± 0.051^d
N V	5.3	1242.8	17.516 ± 0.378^c	0.433 ± 0.040^e
			18.251 ± 0.307^d	0.356 ± 0.033^d
O II	4.8	833.3	14.179 ± 0.839	0.751 ± 0.089
O II	4.8	834.5	15.142 ± 1.751^c	0.661 ± 0.185^e
			17.839 ± 1.178^d	0.379 ± 0.126^d
O III	5.0	833.7	14.607 ± 1.702	0.732 ± 0.181
O IV	5.25	787.7	14.072 ± 1.127	0.799 ± 0.120
O V	5.4	760.2	16.793 ± 1.006^c	0.412 ± 0.107^e
			16.352 ± 1.827^d	0.450 ± 0.194^d
O V	5.4	760.4	16.625 ± 0.730^c	0.498 ± 0.077^e
			17.401 ± 0.455^d	0.418 ± 0.049^d
Fe XII	6.2	1242.0	17.580 ± 0.379^c	0.341 ± 0.040^e
			17.726 ± 0.240^d	0.326 ± 0.026^d

^a Temperature at which line emission is maximum.

^b Calculated for an area of 1800 square pixels (1 pixel $\simeq 1''$).

^c Ignoring data points at the low-density limit.

^d Including data points at the low-density limit.

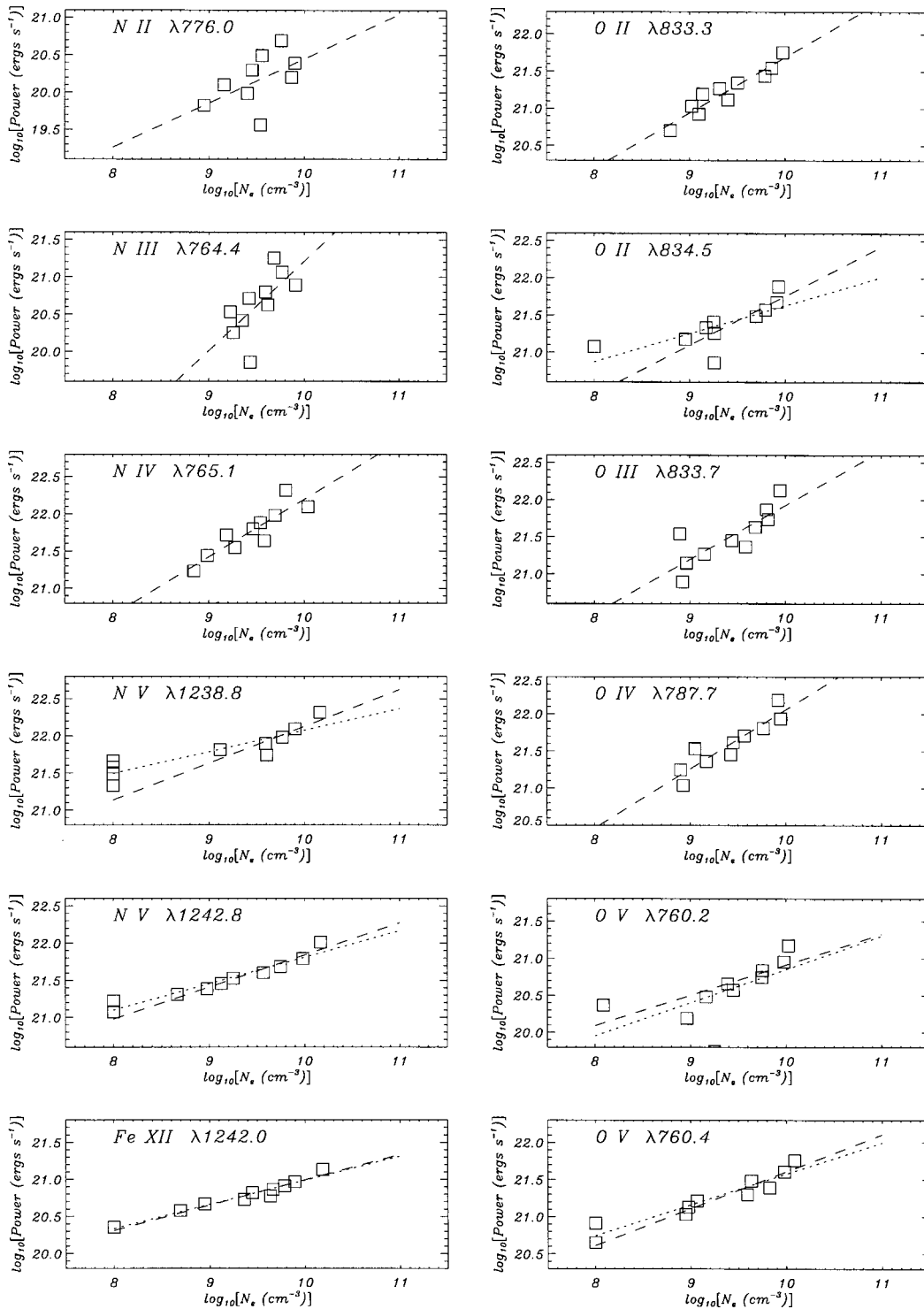


FIG. 5.—Comparison of total emission-line power with electron density (derived from the O IV $\lambda 1399.8/\lambda 1401.2$ line ratio) for 10 different intensity bins in each emission line. Dashed lines show the likely best fit to the data, ignoring any bins at the low-density limit. Dotted lines show fits that include any low-density bins.

Despite the large uncertainties in the density values, it appears from both Figures 4 and 5 that there is a correlation between the intensity and the electron density. Therefore, variations in the intensity cannot be described by an inhomogeneous distribution of many small plasma elements of equal density. Even for our spatially restricted observations of the quiet Sun we must consider a model with plasma elements covering a range of densities. This

variation in density across our field of view compromises the use of O IV] line ratios and complicates the subsequent investigation of physical processes. This is emphasized by Almeky et al. (1989), who note that the density derived from a single line ratio of an inhomogeneous plasma is simply the density of a homogeneous plasma with an identical line ratio. The electron density we calculate should therefore be considered as an “average” value, but accord-

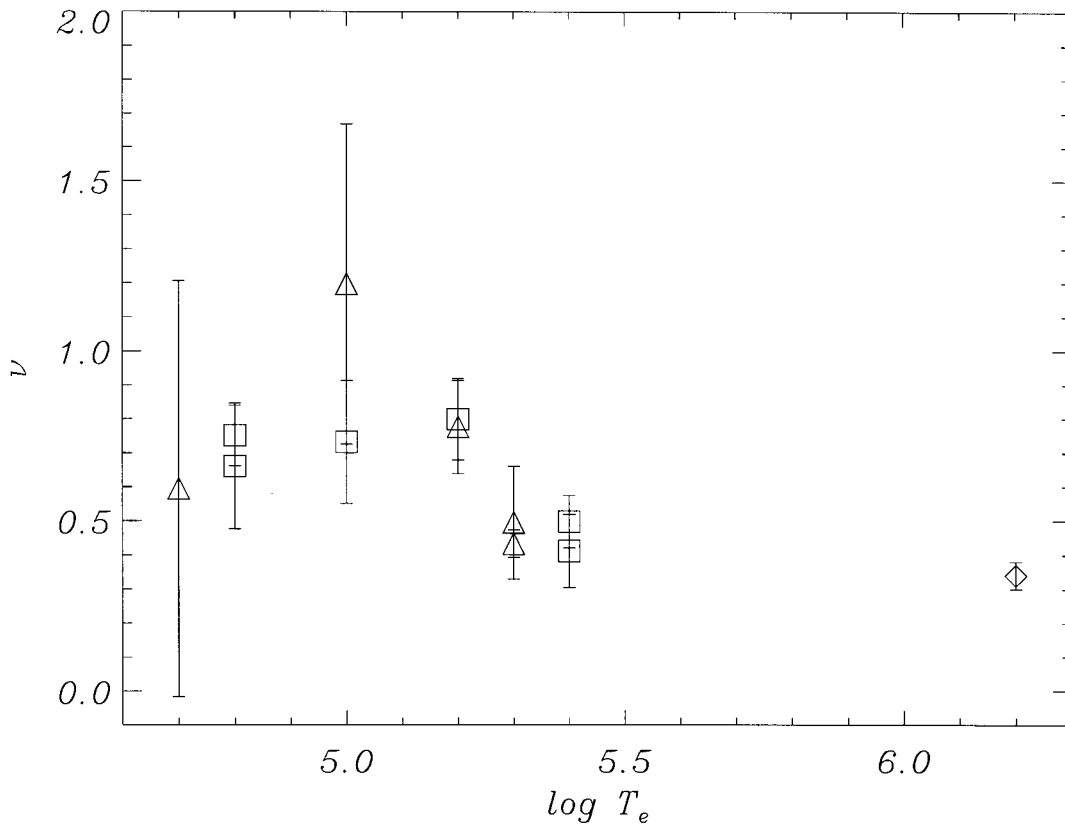


FIG. 6.—Fit parameter ν (see Table 2) as a function of temperature. Triangles denote nitrogen lines, squares denote oxygen lines, and the diamond denotes the Fe XII line.

ing to Almléaky et al. (1989) this will *not be the same* as the volumetric mean density of the observed area.

Strictly speaking, any analysis of the transition region that assumes a single density will only be applicable to groups of elements that are spatially coincident and that have this particular density. Furthermore, SUMER observations have revealed changes in transition region line intensities on timescales as low as 20 s (Judge, Carlsson, & Wilhelm 1997). It is clear that temporal averaging of data can also be a problem. We therefore acknowledge the considerable uncertainties in “average” analyses and the limitations of using density-sensitive line ratios for inhomogeneous plasmas. Unfortunately, for most observations we are restricted by both counting statistics and spatial resolution. Even with the excellent characteristics of the SUMER spectrograph, some kind of averaging is unavoidable, although the problem is significantly reduced relative to previous missions.

6. EMISSION MEASURE DISTRIBUTIONS

As suggested in § 1, one of the most revealing descriptions of the transition region is given by the emission measure distribution. The emission measure can be defined as an integral of the form

$$EM = \int N_e N_H dV. \quad (2)$$

We work in terms of $EM(0.3)$, the emission measure integrated over $\Delta \log T_e = 0.3$ (a typical temperature range for emission-line formation). Defining T_f to be the peak forma-

tion temperature for a given line, we can write

$$EM(0.3)_{T_f} = \int_{\log T_f - 0.15}^{\log T_f + 0.15} N_e N_H dV. \quad (3)$$

It is also possible to define a differential emission measure $\xi(T_e)$ by considering the total power P in an emission line,

$$P = \int G(T_e) N_e N_H dV = \int G(T_e) \frac{\xi(T_e)}{T_e} dT_e, \quad (4)$$

where $G(T_e)$ is the line emissivity calculated in the coronal approximation. We then find that

$$EM(0.3)_{T_f} \simeq \frac{\xi(T_f)}{\sqrt{2}}. \quad (5)$$

It is important to note that we use the “volume” emission measure $\int N_e N_H dV$, which does *not* depend on the geometry of the emitting structures. We can also work in terms of the “height” emission measure, $\int N_e N_H dz$ (or a differential “height” emission measure), which assumes a form for the plasma geometry. In this case a simple plane-parallel atmosphere is often adopted. However, variations of the emitting area with temperature and intensity are likely to occur. This means that true “height” emission measure distributions can have significantly different shapes from “volume” emission measure distributions, and we must be careful to recognize this.

We determine average empirical emission measure distributions using the method described in Griffiths & Jordan (1998). However, we do not include the N v lines in the

calculation of the average EM(0.3) distribution (see § 7). All the atomic physics used to investigate the emission measure distributions have been taken from the CHIANTI database (Dere et al. 1997), and we have adopted the solar photospheric abundances of Anders & Grevesse (1989). There appear to be some small systematic differences between the emission measures derived from the N and O lines, possibly due to abundance effects. When deriving our average distributions, we have placed more weight on the O lines, since these generally have significantly higher count rates. Using the emission lines in our data set, we can determine well-constrained average distributions over the temperature range $4.4 \lesssim \log T_e \lesssim 5.5$.

In Figure 7 we show empirical emission measure distributions from our observations. We show plots for eight different intensity bins, defined to be the eight highest intensity bins in O v $\lambda 760.4$, as shown in Figure 5. In addition to the average distributions, we also show emission measure loci for the individual lines, calculated by assuming that all the emission in a given line is formed at a single temperature. These loci place an upper limit on the emission measure at any temperature. We include loci for all the lines in Table 1, with the exception of the O iv] $\lambda 1400$ multiplet. Two different loci are shown for the Fe xii $\lambda 1242.0$ line. The upper locus is calculated for a photospheric Fe abundance. The lower locus assumes that the Fe abundance is enhanced over the O and N abundances by a factor of ~ 4.5 , typical of the first ionization potential (FIP) effect (Grevesse & Anders 1991). It is not known whether possible FIP-effect abundance variations are caused by enhancement of low-FIP elements (e.g., Fe) or depletion of high-FIP elements (e.g., O and N). For ease of display we show our results assuming that the Fe abundance is enhanced, but we accept that this may not be the case. Figure 7 also includes a plot showing the EM(0.3) distribution and emission measure loci for data averaged over the entire observation.

Many attempts have been made to explain emission measure distributions in the solar transition region. The upper transition region ($\log T_e \gtrsim 5.2$) can be described by simple energy balance models (e.g., Athay 1982). The shape of the observed emission measure distribution in the upper transition region is similar to that predicted for a *single* coronal loop (Antiochos & Noci 1986) and is therefore independent of the area (i.e., number of structures) observed. However, the same energy balance models underestimate the lower transition region emission measures by an order of magnitude or more. This led Antiochos & Noci (1986) to suggest that the emission measure below $\log T_e \sim 5.2$ might be explained by an ensemble of “cool loops” with varying heights and temperatures. In this case the shape of the emission measure distribution is determined by the *relative* populations of the various types of “cool loops.”

Figure 7j compares the average EM(0.3) distributions from four different intensity bins. While the emission measure at $\log T_e \sim 5.2$ varies by almost an order of magnitude from the brightest to dimmest regions, the general shape of the emission measure distribution for $4.4 \leq \log T_e \leq 5.2$ shows only modest variations. The relative invariance of the emission measure distribution for different intensity bins would tend to argue against a distribution of “cool loops” accounting for the lower transition region. Extended regions of the solar surface might be expected to have similar relative “cool loop” populations and consistent emission measure distributions, but the different inten-

sity bins we study give average emission measures from restricted spatial regions. It would therefore be very fortuitous for the derived emission measure distributions to have such similar shapes unless the spatial extent of the cool loops is subresolution (i.e., $< 1''$). This conclusion is reinforced by Figure 8, which compares emission measure distributions from two distinct spatial regions. The high-intensity region consists of only six adjacent pixels in the small, bright feature about halfway up the right-hand side of the intensity maps (see Fig. 1). (This is the smallest region we can study without being affected by the positional variations in different emission lines described in § 2). The low-intensity region is the 60×60 pixel area at the very bottom of each intensity map. Once again we see little variation in the shape of the lower transition region emission measure distribution. The extremely compact nature of the high-intensity region precludes the “cool loop” hypothesis unless the structures are much smaller than 1 pixel.

However, Figure 7 indicates that the EM(0.3) distribution below $\log T_e \sim 5.2$ becomes slightly steeper as the intensity decreases. This is in agreement with Figure 6, which suggests that emission-line power may be most strongly dependent on density at $\log T_e \sim 5.0$. It would appear that the high- and low-intensity emission below $\log T_e \sim 5.2$ arises from generally similar structures, although there are some modest density-sensitive differences.

It is more difficult to investigate the atmosphere above $\log T_e = 5.5$. We have no lines in the range $5.6 \leq \log T_e \leq 6.1$, and only the coronal Fe xii line can be used to constrain the emission measure distribution. We assume an emission measure power law of the form $EM \sim T_e^\alpha$ and investigate possible values of α . Adopting photospheric abundances over the temperature range $5.2 \leq \log T_e \leq 6.2$, α varies from ~ 1.8 in the highest intensity regions up to ~ 2.4 in the lowest intensity regions. Many previous observations have indicated $\alpha \sim 1.5$ in the quiet Sun (e.g., Raymond & Doyle 1981). Our observations seem to suggest higher values of α , but we emphasize that our results are based on the single, rather weak line of Fe xii. There are no obvious first- or second-order blends with this line. However, there remain clear uncertainties over the relative abundances of nitrogen, oxygen, and iron in the transition region and corona. For example, if we assume typical FIP-effect abundances, the value of α varies from ~ 1.1 at high intensities to ~ 1.7 at low intensities. There are obviously significant uncertainties in our values of α , and we cannot say that they are inconsistent with previous results.

While we are unable to determine accurate absolute values of α , our observations do suggest a *decrease* in α with increasing intensity and density. This is independent of the absolute coronal abundance of iron, but could be affected by density-dependent variations in the relative abundances of oxygen, nitrogen, and iron. However, our results are consistent with Raymond & Doyle (1981), who find that α is larger in quiet-Sun cell centers than in the brighter network. They derive their emission measure distributions assuming a plane-parallel geometry, so their results are directly comparable to ours. (Unlike the present work, they do not comment on a change in the distributions below $\log T_e \sim 5.2$.) Their investigation uses emission lines from a range of high- and low-FIP elements and will therefore be subject to some abundance-related uncertainties. However, the similarity between their results and our work suggests that the variation in α is likely to be real.

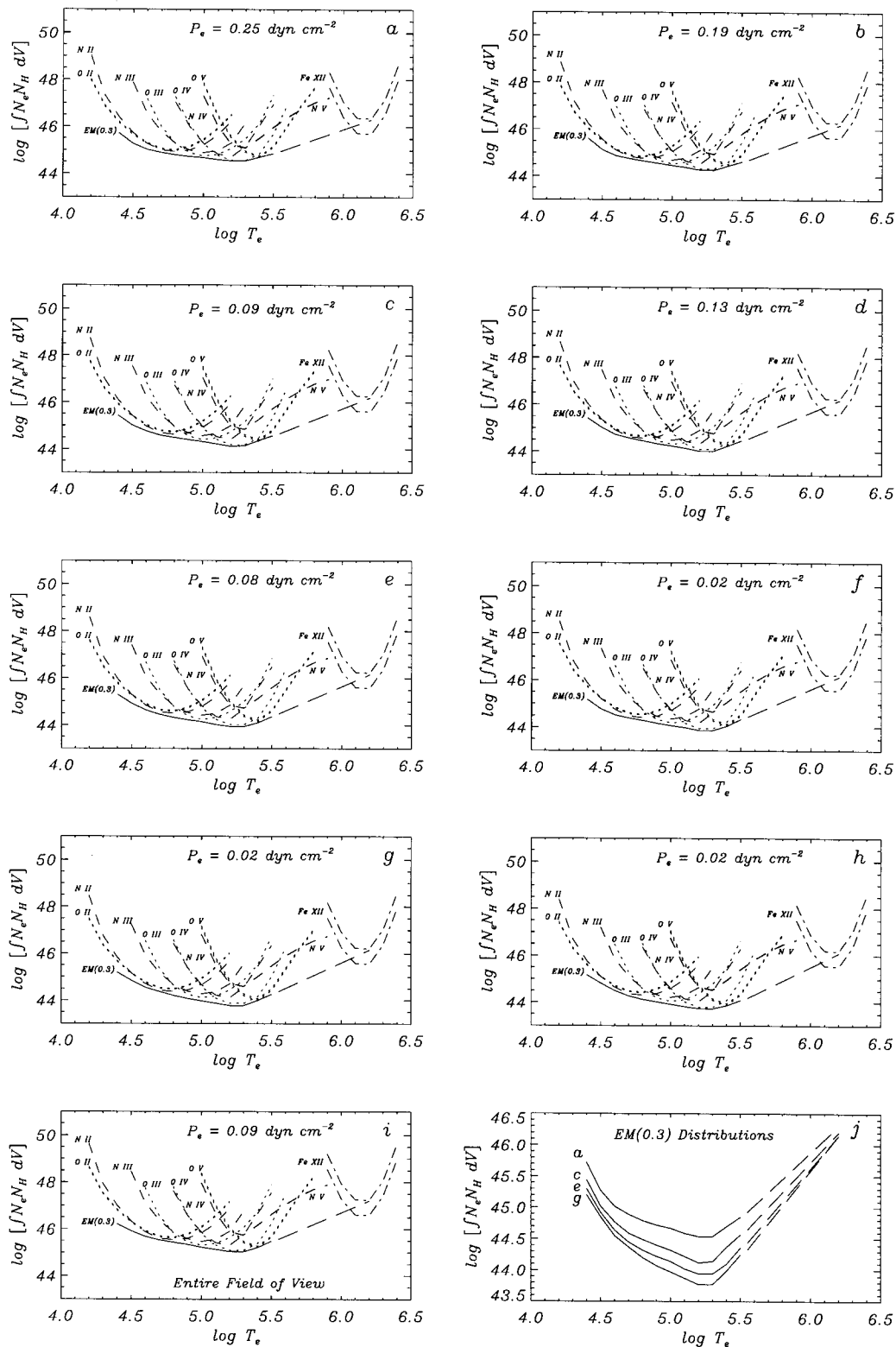


FIG. 7.—(a–h) Empirical emission measure distributions for eight different intensity bins. Emission measure loci for individual emission lines are shown by short-dashed curves (nitrogen lines), dotted curves (oxygen lines), and dash-dotted curves (Fe XII). Two loci are shown for Fe XII $\lambda 1242.0$ to indicate possible FIP-effect abundance variations. The average EM(0.3) distribution is shown by a solid curve for $4.4 \leq \log T_e \leq 5.5$, where it is well constrained. An estimate of the EM(0.3) distribution for $5.5 < \log T_e \leq 6.2$, based on the Fe XII emission and assuming photospheric abundances, is shown by a long-dashed curve. (i) As in a–h, but averaged over the whole field of view. (j) A comparison of the average EM(0.3) distributions for (a), (c), (e), and (g).

Some previous studies have indicated that coronal holes have lower α -values than the quiet Sun, while active regions have higher values (see Raymond & Doyle 1981 and references therein). In other words, there would seem to be an

overall increase in α with intensity. The apparent variation of α in the quiet Sun therefore suggests some important differences between the structures contributing to quiet-Sun emission and those contributing to coronal hole or active-

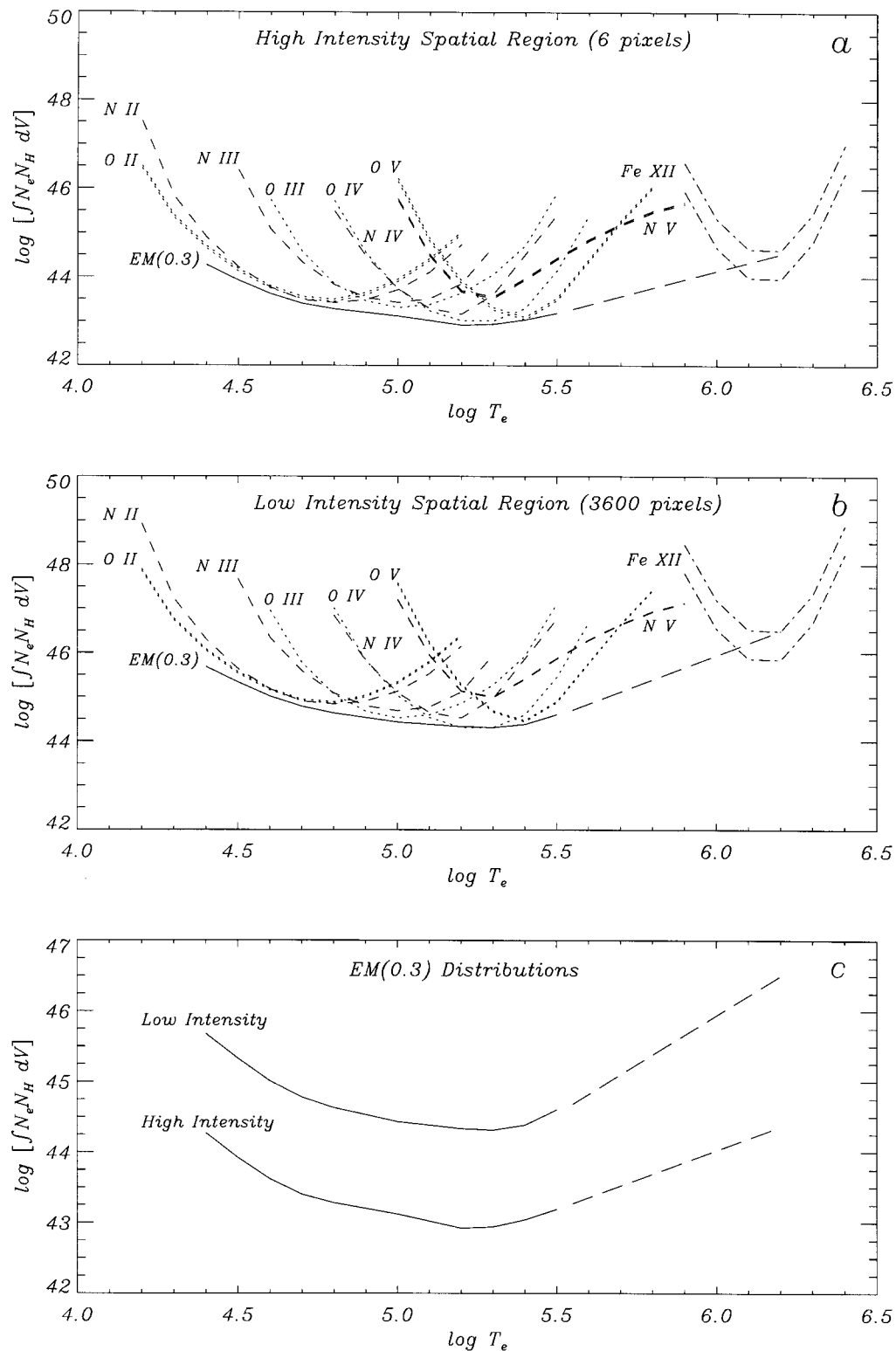


FIG. 8.—Empirical emission measure distributions for two different spatial regions. (a) The emission measure distribution for six adjacent pixels in the small, bright feature about halfway up the right-hand side of the intensity maps. (b) The emission measure distribution for the low-intensity 60×60 pixel region at the bottom of the intensity maps. (c) A comparison of the distributions from (a) and (b). Note that volume-integrated emission measures are shown, so the distribution for the large low-intensity region lies above that for the small high-intensity region.

region emission. We will compare quiet-Sun and active-region data from SUMER in a future paper.

7. N v AND THE Li-SEQUENCE ANOMALY

Higher than predicted line intensities for the Li and Na isoelectronic sequences have been observed on a number of

occasions (e.g., Dupree 1972; Judge et al. 1995). In our observations we find that the N v $\lambda 1240$ emission is much stronger than expected, by a factor of ~ 5 (this is suggested by the emission measure plots in Fig. 7). Figure 9 compares N IV and N v count rates and indicates that this anomaly becomes less pronounced at high intensity. Note that the

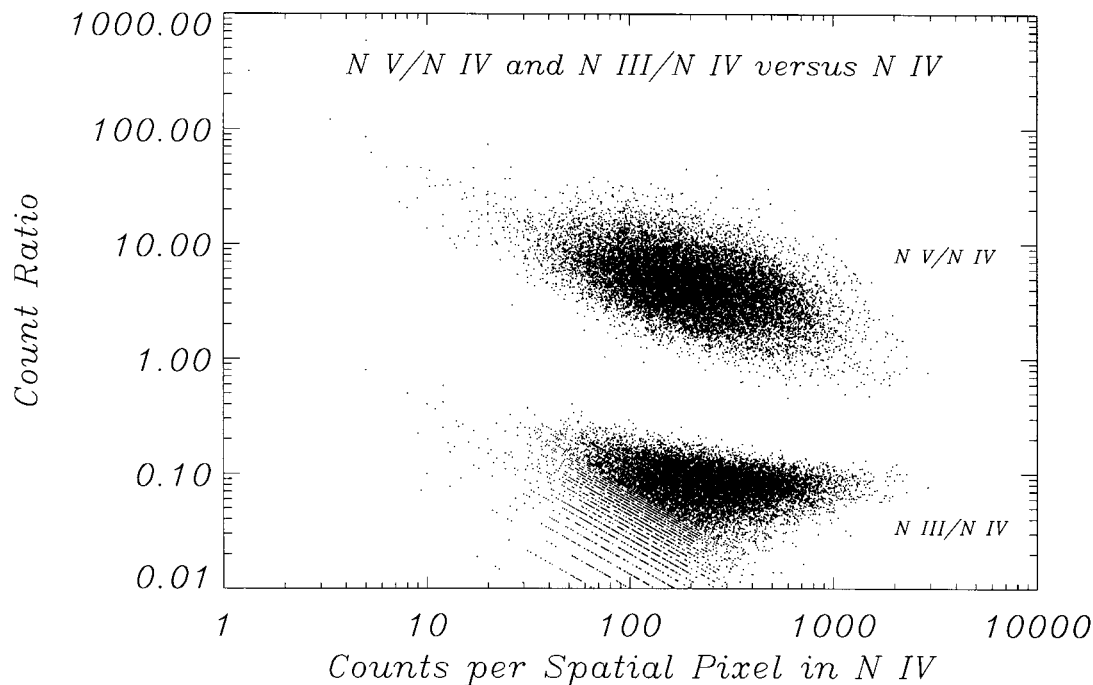


FIG. 9.— $N\text{ V}/N\text{ IV}$ and $N\text{ III}/N\text{ IV}$ count ratios as a function of pixel brightness (counts per pixel for a 60 s integration) in the $N\text{ IV } \lambda 765.1$ line. The respective uncertainties in these ratios are $\sim \pm 0.04$ and $\sim \pm 0.002$.

$N\text{ III}/N\text{ IV}$ line ratio *does not* appear to change significantly with intensity.

The $N\text{ V } \lambda 1240$ lines are bright and commonly observed, and they are therefore important for solar and stellar transition region studies. Consequently, an understanding of the observed anomaly is paramount. A possible source of error is the omission of density dependence of dielectronic recombination from some ionization equilibrium calculations. This includes the work of Arnaud & Rothenflug (1985) (performed at the low-density limit), which we have adopted in this paper. As demonstrated by Jordan (1969), the inclusion of density dependence in dielectronic recombination in the ionization equilibria of the Li and Na sequences can significantly alter the predicted line intensities. However, this possibility is unlikely to explain our results. We observe that the $N\text{ V}/N\text{ IV}$ ratio moves closer to the low-density prediction as the intensity, and therefore the density (see § 5), increases. If the omission of density dependence in dielectronic recombination calculations did explain the apparent $N\text{ V}$ anomaly, we would reasonably expect the deviations to *increase* at higher densities. Dynamical processes that are known to affect ionization equilibrium, such as the acoustic wave interpretation of Hansteen (1993), may therefore be a more likely explanation.

8. CONCLUSIONS

Observations of the quiet Sun taken with the SUMER spectrograph on *SOHO* have been used to investigate several interesting characteristics of the solar transition region. One of the most fundamental conclusions concerns the physical state of the plasma in which transition region emission lines are formed. Our results indicate the presence of structures that extend from the chromosphere, through the entire transition region, and up into the corona. Such structures are particularly evident in the brightest parts of

our field of view. This strongly suggests that much of the emission at transition region temperatures is coming from an intermediate layer in a continuous, stratified solar atmosphere, and not from so-called unresolved fine structures. However, we do see evidence for some transition region emission that is less obviously connected to chromospheric or coronal structures. As discussed by Wikstøl et al. (1998), there are many possible ways to describe the transition region, of which a gravitationally stratified model and “unresolved fine structures” are only two. Our data would seem to indicate that the stratified atmosphere is dominant in the quiet Sun, but it would be foolish to rule out the presence of other structures. In addition, the lognormal distribution of emission-line intensities may suggest that small-scale magnetic fragmentation processes, previously seen in the photosphere, can also be observed at transition region temperatures.

We find empirical relationships between emission-line power and electron density of the form $P = CN_e^v$. The exponent v typically lies in the range ~ 0.3 – 1.0 , and there is some evidence for a peak in the value of v at $\log T_e \sim 5.0$. This is reinforced by the subtle change in the shape of the emission measure distribution as a function of intensity. In addition, the nature of this change may reflect some fundamental differences between the behavior of the transition region in the quiet-Sun and active regions. The SUMER study described in this paper has also been performed on two active regions, and we will compare transition region data from different parts of the Sun in future work.

Despite observing subtle changes in the emission measure distribution, one of our most important conclusions rests on the relative invariance of the distribution shape. In particular, the lower transition region emission measure distribution has a very similar shape for a variety of different intensity and spatial bins. It therefore appears unlikely that

the lower transition region emission can be explained by a distribution of “cool loops” (Antiochos & Noci 1986) unless the size of the structures is much less than 1”.

Our data also indicate higher than expected emission in the Li-sequence N v λ 1240 lines. This conclusion has been reached by a number of previous studies. However, our data suggest that this effect diminishes at higher intensities. In other words, as the density increases, the observed N v flux moves closer to that predicted by the low-density ionization equilibrium calculations of Arnaud & Rothenflug (1985). It is therefore likely that the underlying cause is not the omission of density dependence from dielectronic recombination calculations. A dynamical process in the solar atmosphere (e.g., Hansteen 1993) may be a more appropriate explanation.

In many ways our investigation has served to highlight the difficulties involved with studies of the transition region. The observations discussed in this paper focus on a rela-

tively small portion of the solar surface, and yet we see evidence for large variations in intensity and density. We also see changes in the emission measure distribution and indirect evidence for varying dynamical processes in the transition region. The restrictions associated with analyses of “averaged” data have been discussed, and even with the excellent spectral, spatial, and temporal resolution of SUMER, we are still affected by these difficulties. In summary, it is clear that there is much to learn about even the most fundamental properties of the solar transition region.

The authors wish to thank Giampiero Naletto, Terry Kucera, Philip Judge, and Carole Jordan for their helpful discussions. We also acknowledge many informative comments from the referee, which have improved the clarity of the paper. This research was supported by NASA grant NAG5-7351, and by NSF.

REFERENCES

- Achour, H., Brekke, P., Kjeldseth-Moe, O., & Maltby, P. 1995, *ApJ*, 453, 945
- Almleaky, Y. M., Brown, J. C., & Sweet, P. A. 1989, *A&A*, 224, 328
- Anders, E., & Grevesse, N. 1989, *Geochim. Cosmochim. Acta*, 53, 197
- Antiochos, S. K., & Noci, G. 1986, *ApJ*, 301, 440
- Arnaud, M., & Rothenflug, R. 1985, *A&AS*, 60, 425
- Athay, R. G. 1976, *The Solar Chromosphere and Corona: Quiet Sun* (Boston: Reidel)
- . 1982, *ApJ*, 263, 982
- Bartoe, J.-D. F., Brueckner, G. E., Purcell, J. D., & Tousey, R. 1977, *ApJ*, 16, 879
- Berger, T. E., Schrijver, C. J., Shine, R. A., Tarbell, T. D., Title, A. M., & Scharmer, G. 1995, *ApJ*, 454, 531
- Berrington, K. A. 1984, *At. Data Nucl. Data Tables*, 57, 71
- Bogdan, T. J. 1992, in *AIP Conf. Proc. 267, Electromechanical Coupling of the Solar Atmosphere*, ed. D. S. Spicer & P. MacNeice (New York: AIP), 1
- Bogdan, T. J., Gilman, P. A., Lerche, I., & Howard, R. 1988, *ApJ*, 327, 451
- Brage, T., Judge, P. G., & Brekke, P. 1996, *ApJ*, 464, 1030
- Brueckner, G. E., & Bartoe, J.-D. F., 1983, *ApJ*, 272, 329
- Brueckner, G. E., & Bartoe, J.-D. F., Cook, J. W., Dere, K. P., & Socker, D. G. 1986, *Adv. Space Res.*, 6, 263
- Brueckner, G. E., Bartoe, J.-D. F., & VanHoosier, M. E. 1977, in *Proc. OSO-8 Workshop*, ed. E. Hansen & S. Schaffner (Boulder: Univ. Colorado Press), 380
- Chae, J., Yun, H. S., & Poland, A. I. 1998, *ApJS*, 114, 151
- Cook, J. W., Keenan, F. P., Dufton, P. L., Kingston, A. E., Pradhan, A. K., Zhang, H. L., Doyle, J. G., & Hayes, M. A. 1995, *ApJ*, 444, 936
- Dere, K. P. 1982, *Sol. Phys.*, 75, 189
- Dere, K. P., Bartoe, J.-D. F., & Brueckner, G. E. 1984, *ApJ*, 281, 870
- Dere, K. P., Bartoe, J.-D. F., Brueckner, G. E., Cook, J. W., & Socker, D. G. 1987, *Sol. Phys.*, 114, 223
- Dere, K. P., Landi, E., Mason, H. E., Monsignori Fossi, B. C., & Young, P. R. 1997, *A&AS*, 125, 149
- Dere, K. P., & Mason, H. E. 1993, *Sol. Phys.*, 144, 217
- Doschek, G. A. 1997, *ApJ*, 476, 903
- Doschek, G. A., Feldman, U., & Bohlin, J. D. 1976, *ApJ*, 205, L177
- Dufton, P. L., & Kingston, A. E. 1994, *At. Data Nucl. Data Tables*, 57, 273
- Dupree, A. K. 1972, *ApJ*, 178, 527
- Feldman, U. 1983, *ApJ*, 275, 367
- . 1987, *ApJ*, 320, 426
- Feldman, U., Doschek, G. A., & Mariska, J. T. 1979, *ApJ*, 229, 369
- Feldman, U., & Laming, J. M. 1994, *ApJ*, 434, 370
- Gabriel, A. H. 1976, *Phil. Trans. R. Soc. London, A*, 281, 339
- Grevesse, N., & Anders, E. 1991, in *Solar Interior and Atmosphere*, ed. A. N. Cox, W. C. Livingston, & M. S. Matthews (Tucson: Univ. Arizona Press), 1227
- Griffiths, N. W., & Jordan, C. 1998, *ApJ*, 497, 883
- Hansteen, V. 1993, *ApJ*, 402, 741
- Jordan, C. 1969, *MNRAS*, 142, 501
- . 1996, *Ap&SS*, 237, 13
- Jordan, C., Ayres, T. R., Brown, A., Linsky, J. L., & Simon, T. 1987, *MNRAS*, 225, 903
- Judge, P. G., Carlsson, M., & Wilhelm, K. 1997, 490, L195
- Judge, P. G., Woods, T. N., Brekke, P., & Rottmann, G. J. 1995, *ApJ*, 455, L85
- Lemaire, P., et al. 1997, *Sol. Phys.*, 170, 105
- Mariska, J. T. 1992, *The Solar Transition Region* (Cambridge: Cambridge Univ. Press)
- Raymond, J. C., & Doyle, J. G. 1981, *ApJ*, 247, 686
- Reeves, E. M. 1976, *Sol. Phys.*, 46, 53
- Spadaro, D., Lanza, A. F., & Antiochos, S. K. 1996, *ApJ*, 462, 1011
- Vernazza, J. E., Avrett, E. H., & Loeser, R. 1973, *ApJ*, 184, 605
- Wikstøl, Ø., Judge, P. G., & Hansteen, V. 1998, *ApJ*, 501, 895
- Wilhelm, K., et al. 1995, *Sol. Phys.*, 162, 189
- . 1997, *Sol. Phys.*, 170, 75